ACS APPLIED MATERIALS & INTERFACES

www.acsami.org

Research Article

Visually Hidden, Self-Assembled Porous Polymers for Optical Physically Unclonable Functions

Min Seong Kim and Gil Ju Lee*

Cite This: https://doi.org/10.1021/acsami.2c18737

Read Online

ACCESS | Metrics & More | Article Recommendations | Supporting Information

Downloaded via PUSAN NATL UNIV on January 15, 2023 at 02:22:03 (UTC).
See https://pubs.acs.org/sharingguidelines for options on how to legitimately share published articles.

ABSTRACT: Owing to the advancement of security technologies, several encryption methods have been proposed. Despite such efforts, forging artifices is financially and somatically becoming a constraint for individuals and society (e.g., imprinting replicas of luxury goods or directly life-connected medicines). Physically unclonable functions (PUFs) are one of the promising solutions to address these personal and social issues. The unreplicability of PUFs is a crucial factor for high security levels. Here, this study proposes a visually hidden and self-assembled porous polymer (VSPP) as a tag for optical PUF systems. The VSPP has virtues in terms of wavelength dependency, lens-free compact PUF system, and simple/affordable fabrication processes (i.e., spin coating and annealing). The VSPP consists of an external saturated surface, which covers the inner structures, and an internally abundant porous layer, which triggers stochastic multiple Mie scattering with wavelength dependency. We theoretically and experimentally validate the unobservability of the VSPP and the uniqueness of optical responses by image sensors. Finally, we establish a wavelength-dependent PUF system by using the following three components: solid-state light sources, a VSPP tag, and an image sensor. The captured raw images by the sensor serve as "seed" for unique bit sequences. The robustness of our system is successfully confirmed in terms of bit uniformity (~0.5), intra/interdevice Hamming distances (~0.04/~0.5), and randomness (using NIST test).

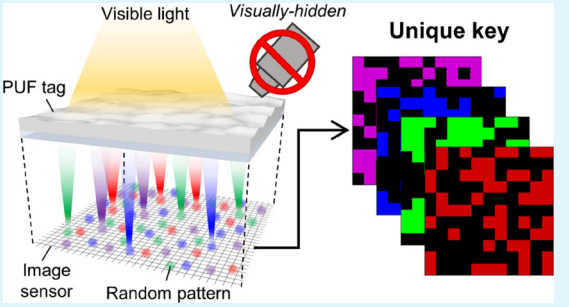

KEYWORDS: *physically unclonable function, optical physically unclonable function, porous medium, multiple Mie scattering, hardware-based security*

1. INTRODUCTION

Recently, the explosive increase of counterfeit consumer products has caused serious social problems, such as huge economic losses, threatening human safety by replicas of luxury goods,[1−4] and fake medicines/medical devices.[5−7] In addition to these physical damages, digital information including confidential and private data has been notably attacked for the predatory and abusive purposes in most areas of modern society.[8−11] To protect us from these off-line/on-line attacks, a thorough authentication process plays an important cryptographic primitive validating the identifier for authentic items and authorized users.[12,13] In this context, strong identifiers have been intensely required and developed in various ways.[14−18] Among them, physically unclonable functions (PUFs), i.e., nonalgorithmic one-way functions, have emerged as an unbreakable identifier because PUF-based tags consist of unreproducible elements resulting from a random fabrication process.[19−24] In every manufacturing process, the stochastic feature in the process generates a truly unique PUF-based tag by even the same process.

Based on the unique feature of PUF-based tags, each PUF possesses a unique pair of input and output, which is called a challenge and response pair (CRP). Such one-on-one matching of CRP allows working of the PUF as a digital fingerprint. In principle, the two levels of PUF strength (i.e., weak and strong PUFs) are determined by the number of CRPs that can be generated in a single PUF-based tag, thus generally the size increase of the tag is the easiest way to raise the number of CRPs.[20] The strong PUF, which has a large repertoire of CRPs, can use each CRP only once, in other words, the output response is discarded once read from the database.[20] To satisfy the condition for strong PUFs, optical PUF systems have been promising since the tags in optical PUFs exploit not only the spatial domain (i.e., the physical domain of tag) but also the spectral domain in a single tag. This advantage enables the implementation of strong PUF with small sized tags. However, the optical PUFs generally have bulk and complex configurations owing to essential apparatus such as polarizers, objective lens, and requiring certain equipment (Table S1).[25−30] To address this issue, a few research studies proposed the optical PUF systems allowing

Received: October 18, 2022
Accepted: January 3, 2023

© XXXX American Chemical Society

lens-free operation.[31] In general, the morphology of these PUF tags could be found by optical and/or electron microscopy,[29−31] probably offering vulnerable points in the PUF system potentially. A strong PUF system should minimize the potential replicability or predictability on the tags in the PUF system.

Herein, we propose a lens-free, veiled, wavelength-dependent optical PUF system based on a visually hidden and self-assembled porous polymer (VSPP) with an affordable simple process to address current challenges: (1) complicated configuration of optical PUFs, (2) observable structure of PUF tags, and (3) increasing the number of CRPs. First, our system consists of only three components: solid-state light sources, a VSPP film, and an image sensor. Also, the PUF tag, which is the VSPP, is fabricated using a simple spin-coating process.[32] The spin coating process, which is one of the semiconductor processes, has strengths compared to other approaches in terms of fabrication difficulty, cost, and time consumption for tag manufacturing (Table S2).[33−36] During spin coating, the phase inversion of the solution leads to the generation of VSPP owing to the evaporation rate difference of composites. This porous layer generation tendency depends on the nonsolvent ratio in the solution. While spin-coating, air voids in the polymeric structure derive from the nonsolvent, therefore this solubility difference for two liquids can generate the sponge-like layer. The sponge-like structure, which has tons of air voids in the nanoscale, differently scatters an incident light depending on the wavelength. Such iridescently scattered light pattern captured by an image sensor becomes the seed of the random key. These captured images are unique and independent from each other (Figure S1). The spectral difference considerably increases the size of CRP because the VSPP shows a completely different optical response even at the incident wavelength with 10 nm intervals. Owing to the stochastically generated pores in the VSPP tag (i.e., the same process and unpredictable nanosized morphology), one tag can be discarded immediately after the certification process (i.e., a disposable tag). This one-shot authentication characteristics strongly enhances the entire cryptographic system. To produce an unreproducible key from a raw image, five image-processing steps were executed: (1) noise reduction, (2) resizing, (3) application of a threshold intensity value of 85%, (4) binning, and (5) two-channel von Neumann debiasing.[31] In addition, the performance of the PUF (i.e., randomness, bit uniformity, and inter/intradevice Hamming distance (inter-HD/intra-HD)) is evaluated to highlight the proposed PUF system.

2. RESULTS AND DISCUSSION

2.1. Producing Random Bit Sequences. The VSPP has self-assembled/complex nanoporous structures and its spectrally unique responses serve as the seed of the PUF. Figure 1 shows the schematic illustration for the VSPP-based optical PUF system. The VSPP-based PUF tag consists of two layers: saturated layer and porous layer. These hierarchical layers prevent observing the exact shape of the internal pores even when both optical and electron microscopes are used. For optical microscopy, the nanopores in the VSPP promote multiple Mie scattering, hence the VSPP is a highly scattering medium that forces nonstraight propagation of the light. In addition to scattering, the observation itself on nanopores is limited by Abbe's diffraction limit.[37] According to the diffraction limit theory, an object with a size smaller than 200 nm cannot be observed using the visible light sources from

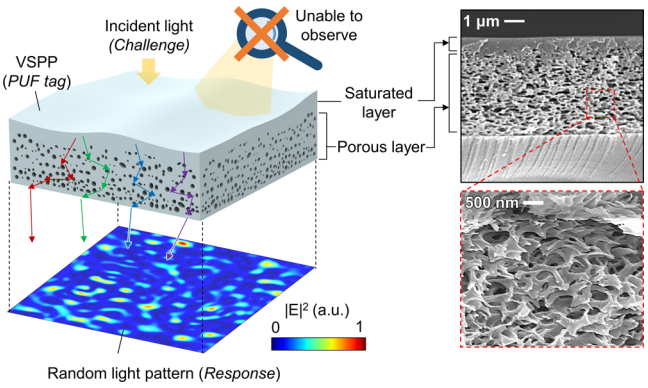

Figure 1. Schematic illustration of the VSPP-based PUF system. Incident light and random light pattern are "challenge" and "response", respectively. VSPP has the saturated layer, it is unable to see the morphology of the porous layer. Film unexpectedly scatters the incident light owing to stochastically generating air voids at the porous layer. Additionally, these nanostructures are unique and dissimilar under the same procedure step. Inset shows the cross-sectional scanning electron microscopy image of VSPP.

400 to 700 nm in wavelength (Figure S2). In the VSPP, although the pores with a larger size than 200 nm exist, smaller pores than 200 nm are also distributed. The detailed structural analyses are discussed in the Section 2.2. Therefore, even high-resolution optical microscopies for investigating of highly scattering medium (i.e., skin), such as confocal laser scanning microscopy, are unfeasible to identify the exact structure of VSPP.[38−40] Scanning electron microscopy (SEM) can resolve the internal pores, however, the top saturated layer completely screens the observation of SEM on the internal pores.

The only way to manifest the characteristics of VSPP is irradiating light on the VSPP and capturing the spectral response by an image sensor. Once light is incident on the VSPP layer, the disordered nanoscale pores in the VSPP cause multiple Mie scattering. The scattered light captured by the image sensor exhibits unique light patterns depending on the wavelength (Figure S3).[41,42] Thus, spectrally separated patterns of VSPP are achieved by a commercial image sensor and light sources (Figure S4). Our system exploits laser diodes with four different colors (violet, blue, green, and red) as the light sources. A single VSPP-based PUF tag offers four unique patterns changing the color channel. After the capturing process, the collected images are post-processed for bit generation (Figure 2). The assembled visual data possess external and/or intrinsic noise, and a denoising filter (a nonlocal means filter) is employed to reduce the noise[43] (Figure S5). The noise-reduced RGB image set is converted into grayscale images. The converted image set is resized from 3664 × 2748 to 256 × 256 pixels to alleviate the computation time. The computing time has decreased about four times for rescaled raw image data (Figure S6). To minimize the influence of the intrinsic noise, 85% of the individual intensity values are applied to each image. The standard for threshold value is described in Figure S7. Subsequently, binning is performed (Figure S8). The bit uniformity of nonprocessed bitstream indicates an extremely low value (i.e., biased), and the two-channel von Neumann debiasing facilitates satisfying the bit uniformity ~0.5. As a response, among all the bits, the first 190 bits are selected because of the consistency of the final response length (Figure S9).

https://doi.org/10.1021/acsami.2c18737
ACS Appl. Mater. Interfaces XXXX, XXX, XXX−XXX

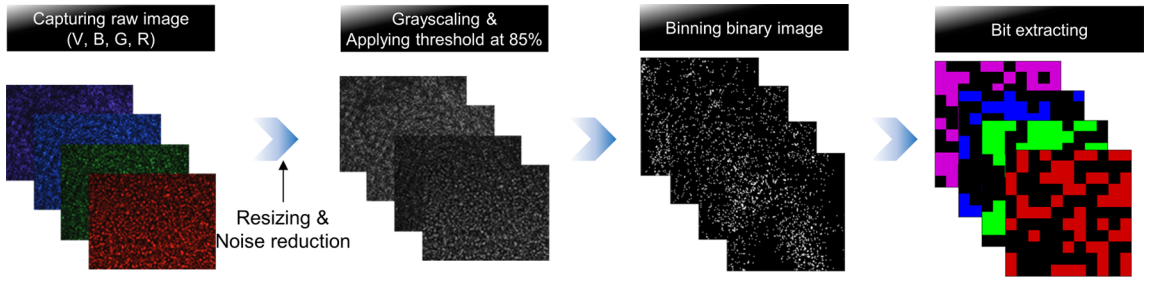

Figure 2. Whole key generation process. Propagated light through the self-assembled polymeric film, which exhibits random and unique patterns. Obtained images are denoised and resized into 256 × 256 pixels. A single percentile value of 85% is applied to select the proper pattern array from the remaining influence of noisy surroundings. Binning is executed after the digitizing stage. Two-channel von Neumann extractor has debiased from the biased bit sequence.

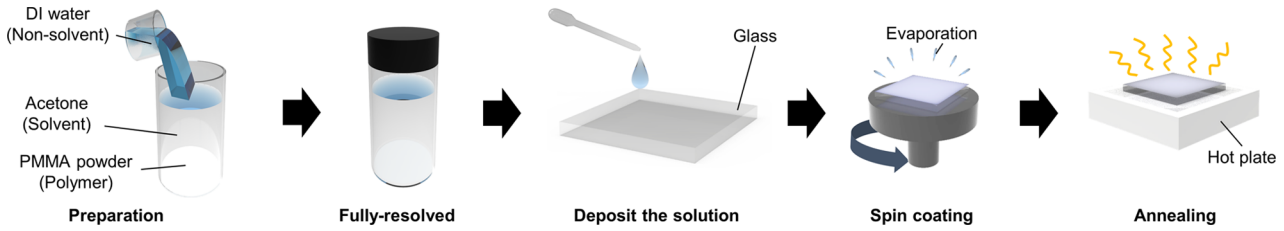

Figure 3. Self-assembly method for fabricating VSPP films. Phase inversion method can simply generate the random porous layer. Undergoing an evaporation step, a dissolved polymer in a solvent becomes a polymeric structure, and a nonsolvent transforms into randomly distributed pores in PMMA network.

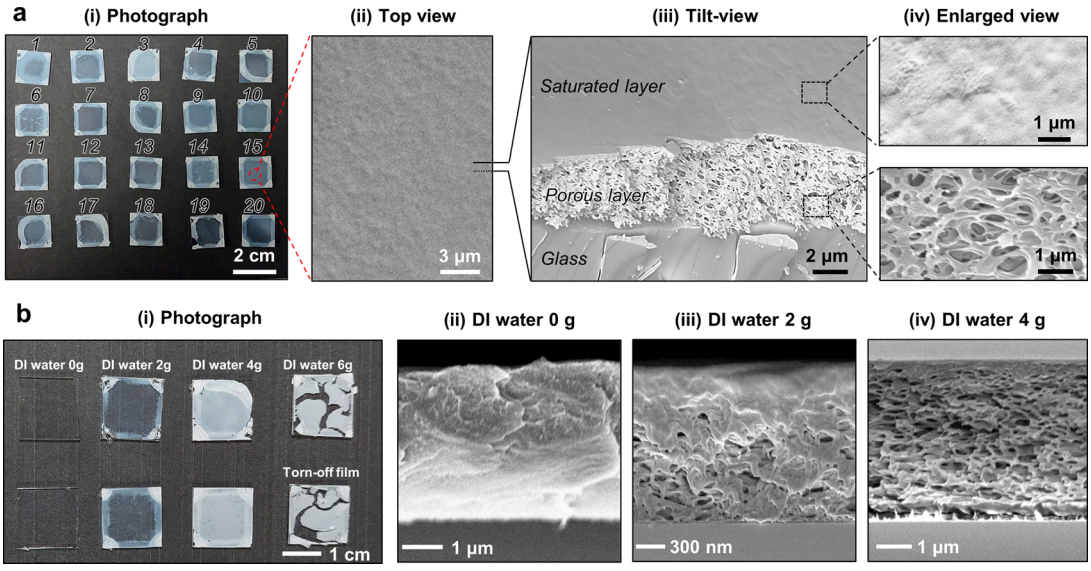

Figure 4. Experimental analysis of the self-assembled porous polymer. (a) Morphological characteristics of VSPP. (i) Photograph of the entire VSPP. Each glass substrate is diced based on a rectangular shape of 1.5 × 1.5 cm^2; the same fabrication process is repeated 20 times. (ii) Top view of VSPP, using scanning electron microscopy (SEM). Owing to the saturated layer on the top, the inner porous layer is veiled. (iii) Tilt-view of SEM more easily distinguish the two layers, (e.g., saturated layer and porous layer). (iv) More enlarged view of the saturated layer (upper) and porous layer (lower). (b) Nonsolvent dependence for stochastic pore generation in VSPP. Each sample has different DI water amounts (i.e., 0, 2, 4, and 6 g). (i) Appearances of the samples. More than 4 g of DI water, the film separates from the glass substrate during the spin-coating process. Cross-sectional view of only-solvent (ii), 2 g (iii), and 4 g of DI water (iv).

2.2. Stochastically Generated Porous Layer. The VSPP is fabricated using a phase-inversion method, which is a self-assembly, cost-effective, and stochastic process. Figure 3 shows the fabrication process of VSPP on a glass substrate. First, the mixture of deionized (DI) water, acetone, and poly(methyl 2-methylpropenoate) (PMMA) powder is prepared. Next, ultrasonication resolves the polymer into the solvent (i.e., acetone) and nonsolvent mixture (i.e., DI water). The fully resolved solution is spin-coated on the substrate and annealed using a hot plate. In the rotation stage, the evaporation rate difference of acetone and DI water causes the generation of porosity. The rapid evaporation of the volatile acetone allows the phase separation of PMMA from the DI water.[44] The phase separation solidifies the PMMA dissolved in the solution again, while DI water remains as droplets in this moment. In other words, the network of PMMA is already formed before DI water evaporation. After sufficient time, the network of

https://doi.org/10.1021/acsami.2c18737
ACS Appl. Mater. Interfaces XXXX, XXX, XXX−XXX

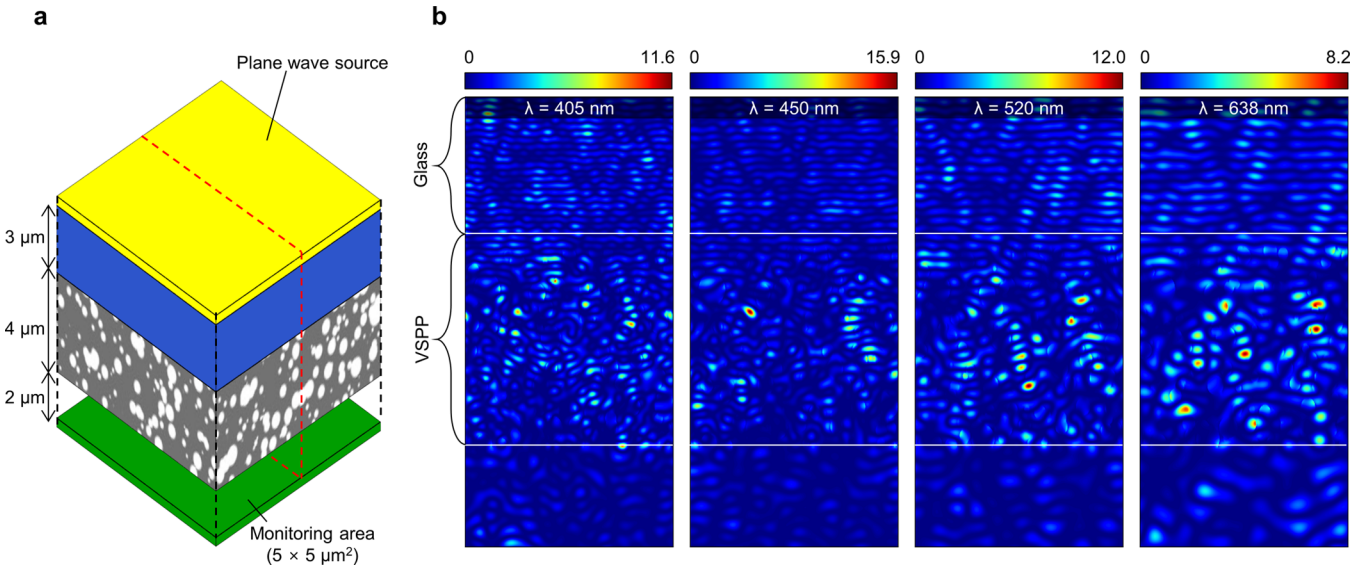

Figure 5. Theoretical simulations for the investigation of optical phenomena in VSPP. (a) Simulation model of the VSPP. FDTD simulation domain comprises a glass, PMMA, and free space. Red dashed line indicates an observation plane. (b) Two-dimensional final field of the FDTD simulation results depending on four wavelengths. In the porous PMMA, propagating lights interfere with each other, and therefore, intensity peaks appear in the PMMA layer.

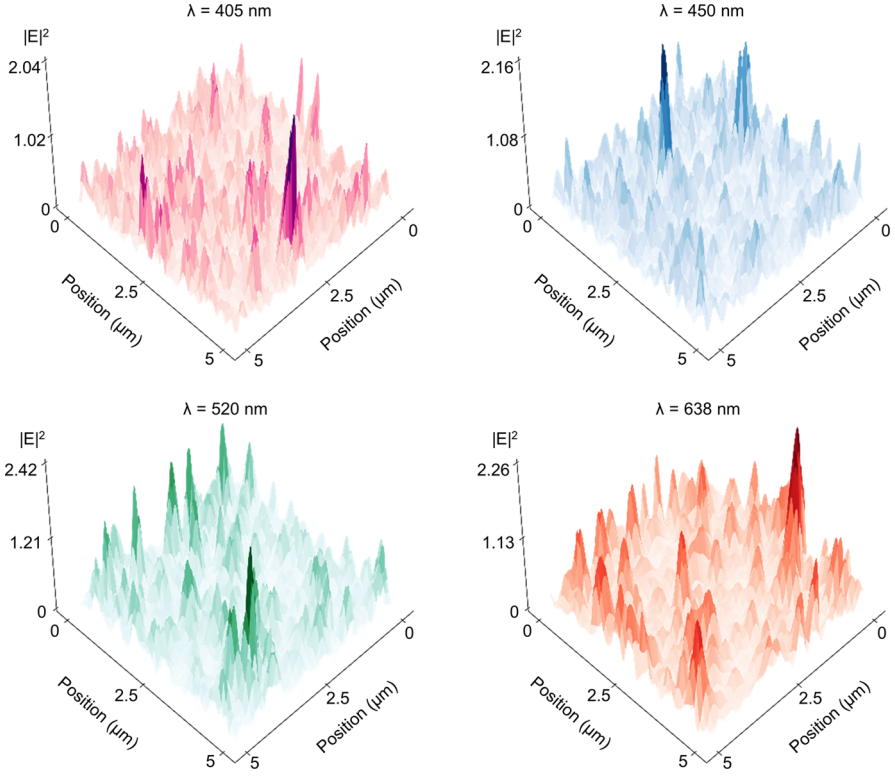

Figure 6. Electric field intensity profiles at the monitoring area for four wavelengths such as 405, 450, 520, and 638 nm. Results show the wavelength dependency of the electric field through a porous polymer layer.

PMMA is only left including air voids corresponding to droplets of DI water.

This method facilitates the stochastic generation of abundant nanopores in VSPP. The detailed fabrication method is described in the Section 4. The photograph in Figure 4a-(i) displays the fabricated 20 VSPPs using the previously described process. The scattering of nanopores hinders to observe the detailed geometry of nanopores by optical microscopy (Figure S10). Furthermore, such a hierarchical structure of VSPP is impregnable against high-resolving power microscopy such as SEM and atomic force microscopy (AFM). From the top view of SEM image, a smooth surface (i.e., saturated layer) is only observed (Figure 4a-(ii); top view). A tilt-view of SEM reveals the two structures more obviously (Figure 4a-(iii); tilt-view). The enlarged views of Figure 4a-(iv) display the saturated layer (upper) and porous layer

https://doi.org/10.1021/acsami.2c18737
ACS Appl. Mater. Interfaces XXXX, XXX, XXX−XXX

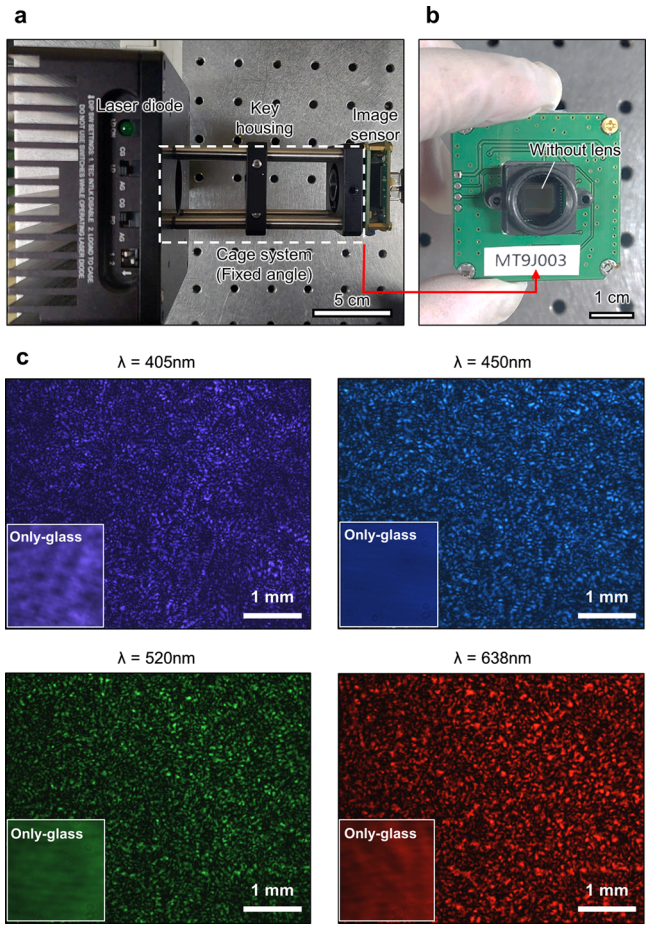

Figure 7. Experimental measurement setup. (a) Cage system tightly fixes the entire optical components, therefore the angular variance is eliminated. (b) A built-in lens of the image sensor is removed for the lens-free system. (c) Spectrally separated images in a single sample under four different light sources. Compared to the images from the only-glass, the VSPP film randomly scatters the incident light.

(lower) in the VSPP film. The entire thickness of the VSPP is ~4 μm, which is the proper thickness for light penetration. A high thickness with abundant pores hinders the capturing process of the spectral response using the image sensor owing to low transmittance (Figure S11). Quantitative morphological analyses are performed based on the microscopic observations (Figure S12). This result apparently exhibits that the average size of pores is ~185 nm and the pores are closely packed (i.e., the mean value of nearest neighbor distance = ~151 nm). The surface roughness of VSPP is ~24 nm in average.

These saturated top surface and internal porous structures can prevent the duplication of the structure in the VSPP film and preclude the expectation of an image captured using an image sensor owing to the complicated light−matter interactions in the porous layer. However, as the geometrical analyses display, the VSPP film has also a nanoscaled groove surface. To reveal the geometrical influence, a two-dimensional finite-difference time-domain (FDTD) method is conducted for each case: groove-only and pore-only layers (Figure S13a). Although the VSPP has a nanoscaled groove, the optical responses depending on the wavelengths are analogous, which is not proper as a seed for random bit sequences. On the contrary, the optical responses of the discretionally distributed porous medium are fully different according to the wavelengths (Figure S13b).

The weight ratio of the nonsolvent (i.e., DI water) in the solution influences the porous layer generation. Figure 4b shows the appearances of samples with the variation of the DI water amount (i.e., 0, 2, 4, and 6 g) in the photograph and SEM images. The sample without DI water completely saturates on the glass substrate. This sample exhibits a clear surface. The sample with the DI water of 2 g has some pores in the layer but not much as the VSPP (i.e., 4 g DI water). In our VSPP, abundant pores trigger to a multiple Mie scattering, which is the main mechanism of wavelength-dependent light patter. As a result, 4 g DI water is a better option than other samples with the DI water of 0 or 2 g. As the amount of DI water increases, the sample is torn-off from the substrate during the spin-coating process. This may originate from the breaking of the PMMA network by a large size of air void from too much water amount. Therefore, the amount of DI water considerably affects the pore generation in the VSPP. The optimal weight ratio of the mixture is 50 g of acetone, 4 g of DI water, and 5 g of PMMA.

2.3. Theoretical and Experimental Analysis. The VSPP exhibits a three-dimensional structure; hence, three-dimensional FDTD simulations are performed to visualize the light propagation in porous medium and verify the wavelength dependency of Mie scattering. To mimic the VSPP, the simulation structure comprises a 3 μm-thick glass and a 4 μm-thick porous PMMA layer. Although the simulation cannot reflect the measurement in real-world scale, the simulation is sufficient to analyze the optical phenomena in VSPP.[45−48] The monitored area exhibited a rectangular area of 5 × 5 μm^2. Figure 5 shows the simulation domain and environment setting. As shown in Figure S13, the pore-only layer exhibits a spectrally different field pattern compared to those of the groove-only layer. Therefore, a three-dimensional pore-only layer is utilized for FDTD simulation for simple calculation. In this simulation, the model for VSPP has 4000 air voids and the PMMA matrix. The number of pores is set to the volume of bulk PMMA divided into the average pore volume from the results of geometrical analyses. The VSPP modeling method in the computing space and additional calculation result is illustrated in Figure S14a−c.

Figure 5b shows the electric field intensities for the four wavelengths in the cross-sectional view marked by a red dashed line in Figure 5a. These results display that intense spots caused by weak light localization are different depending on the wavelength. The weak light localizations occur within the porous layer owing to an optical interference between counter-propagating waves.[49] Since the optical interference is a function of wavelength, the light localizations become different under four wavelengths. These spectrally varied localizations induce unique characteristics, such as peak location, value, and counts, for each color channel in the monitoring area (Figure 6). Furthermore, this structure generates unique responses for the wavelengths at 10 nm intervals (Figure S15). Each calculated electric field (E-field) profile is independent (Figure S16). The sensitivity to angles is also excellent, hence these features enable a large CRP repertoire for a single sample (Figure S17a,b).

In addition, the physical properties (i.e., refractive index and thickness) of the film are also analyzed. At the same simulation space, the background refractive index corresponding to the polymer changes from 1 to 1.5 and the thickness of the porous

https://doi.org/10.1021/acsami.2c18737
ACS Appl. Mater. Interfaces XXXX, XXX, XXX−XXX

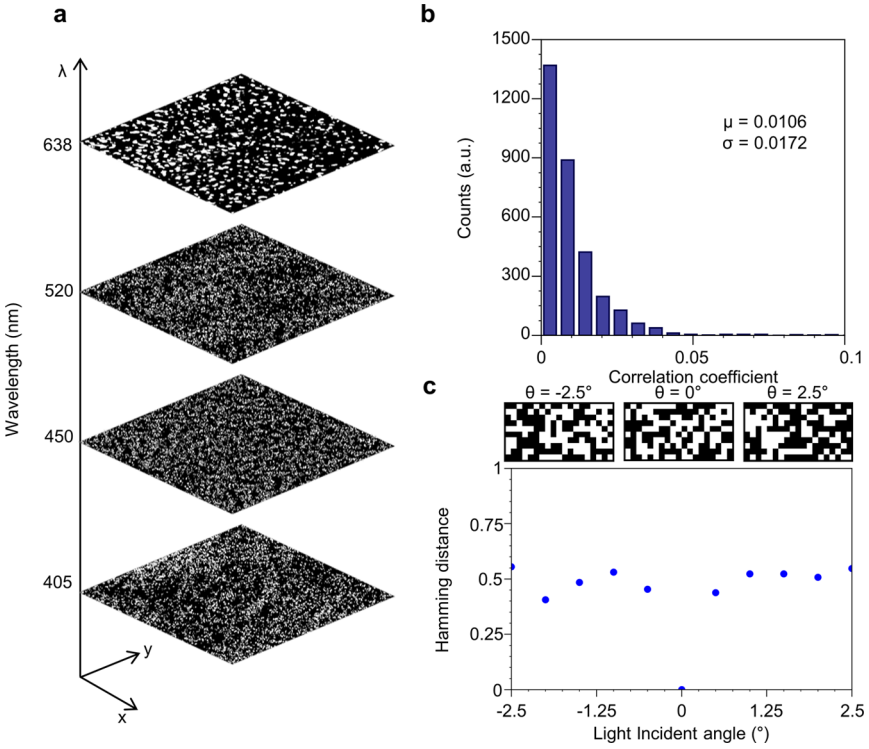

Figure 8. Wavelength and angular dependence of VSPP-based PUF tag. (a) Binary images for four wavelengths before the von Neumann debiasing algorithm. (b) Correlation coefficients for all seed images indicate extremely low values, therefore the seed of bitstream is spectrally separated. (c) HD for final response bitmaps according to various incident angles. Above bit maps show the extracted final bits for three incident angles. Using the tilt-setup, the final extracted bits show an independent bitmap (i.e., HD value of ∼0.5). Figure S17 shows more detail theoretical and experimental results.

layer varied from 1 to 5 μm, respectively. From the monitoring results, the mean peak values at each channel is shown in Figure S14d. As the difference of refractive indices increases, the mean peak intensity saturates near the value of 2. Hence, the refractive index of PMMA (∼1.5) is sufficient to cause adequate peaks which can be used as the seed of random bitstream at the monitoring area. Figure S14e shows the average number of peaks at each channel of monitored result. At the monitoring area, the simulated field results are applied the threshold value of 85% and peak number is counted. All simulated threshold-applied images are shown at Figure S18. The simulation results indicate that the propagating light in the porous layer is scattered and uniquely localized depending on the wavelength. Moreover, the physical properties of the porous layer (i.e., refractive index and thickness of porous layer) are appropriate to provoke the multiple scattering. Thus, these computational studies support that the VSPP possesses strong wavelength dependency owing to multiple scattering.

Figure 7a displays the measurement setup, where three components are aligned by a cage system for the mechanical stability. Figure S19 shows a schematic illustration of the estimation setup for the experimental validation of VSPP-based PUF tag. The demonstration system comprises the following three optical components: laser diodes (LDM56/M, L405P20, L450P1600MM, L520P50, and L638P040, Thorlabs, USA), VSPP-based PUF tag, and image sensor (MT9J003, Arducam, China). The VSPP film is fixed in a key housing. Owing to the cage system, the relative angular variance cannot affect to this setup. Also, our system uses a lens-removed image sensor (Figure 7b). Using this setup, seed images are obtained at the same observation position for four color channels (Figure 7c). Figure S20 shows all the obtained images from this setup. Each image manifests a different light pattern to each other, i.e., unique responses in a single tag. The binarized images of the obtained seed patterns also highlight the distinct peak positions of each seed image (Figure 8a). Figure 8b shows the correlation coefficients of all raw image (i.e., 80 images from 20 tags and 4 wavelengths). The correlation coefficient between the seed images is <0.05, hence, the obtained visual data set is independent of each other. In addition, individual VSPP-based PUF tags present distinct seed patterns, and the seed patterns demonstrate extremely low correlation. The correlation coefficient for all raw images is given by:

$$R_{ij} = \frac{C_{ij}}{\sqrt{C_{ii}C_{jj}}}$$

where R is the coefficient matrix and C is the covariance matrix.

The raw image data have the dimension of 2 therefore the individual array flattened to a one dimensional vector. The formula mentioned above applies for the flatten 1D array and the value of R_{10} ($=R_{01}$) is represented to the correlation coefficient.[50]

In principle, a multicolored channel can increase the repertoire of CRP and is useful to develop a strong PUF system.[20] Since the outstanding wavelength-sensitivity of the porous structure is theoretically proved, our study provides the feasibility for a strong PUF using a VSPP-based PUF tag and wavelength-variable light source.[51,52]Figure 8c shows the angular dependency of the VSPP which can improve the repertoire of CRP. The incident angle varies, and final

https://doi.org/10.1021/acsami.2c18737
ACS Appl. Mater. Interfaces XXXX, XXX, XXX−XXX

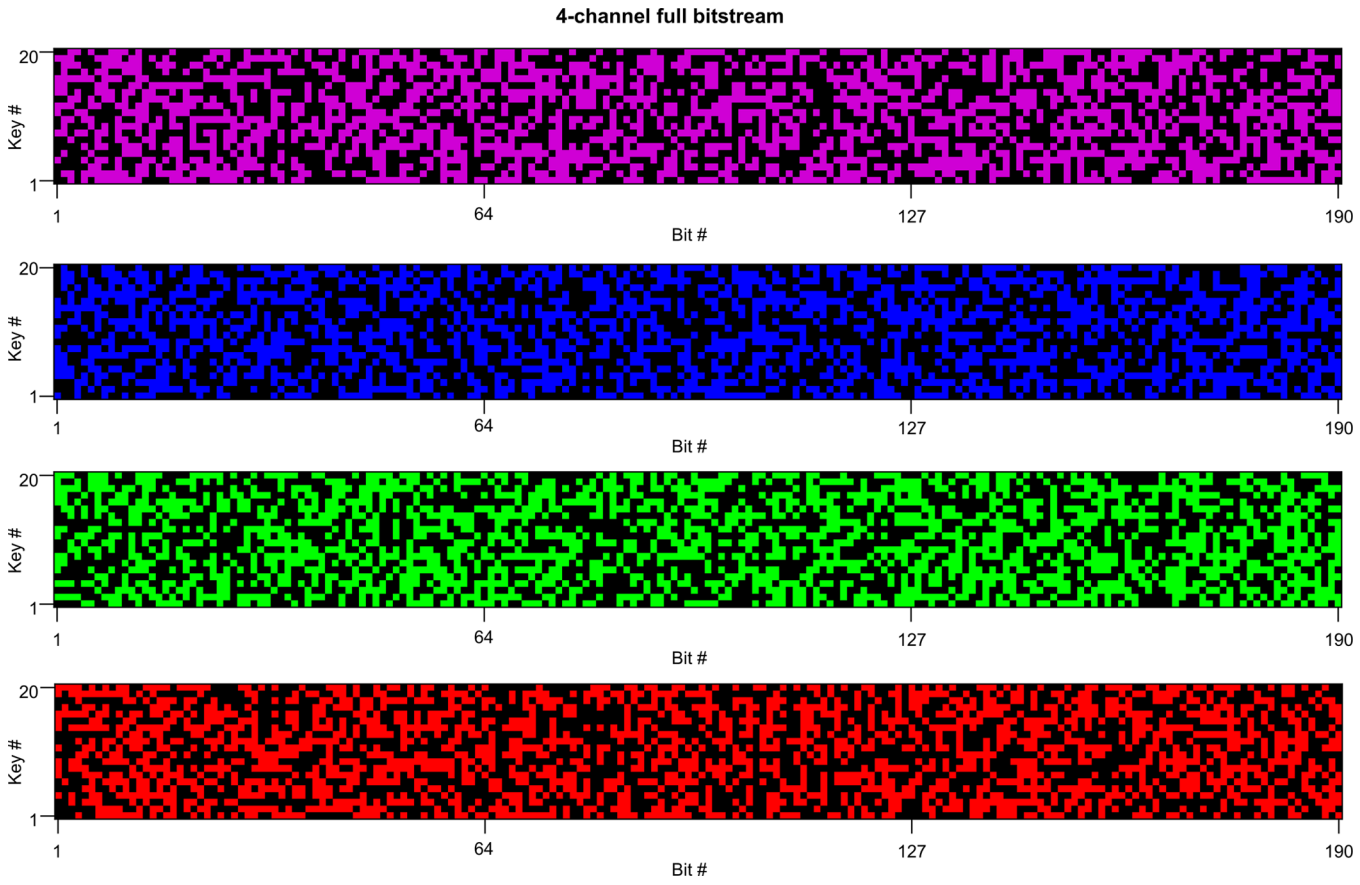

Figure 9. Entire bit sequence from four different color sources. A total of 80 bitstreams produced for optical PUF. Laser diodes of 405 (violet), 450 (blue), 520 (green), and 638 nm (red) are used to generate the random key. Final responses of each color are painted to their color channel.

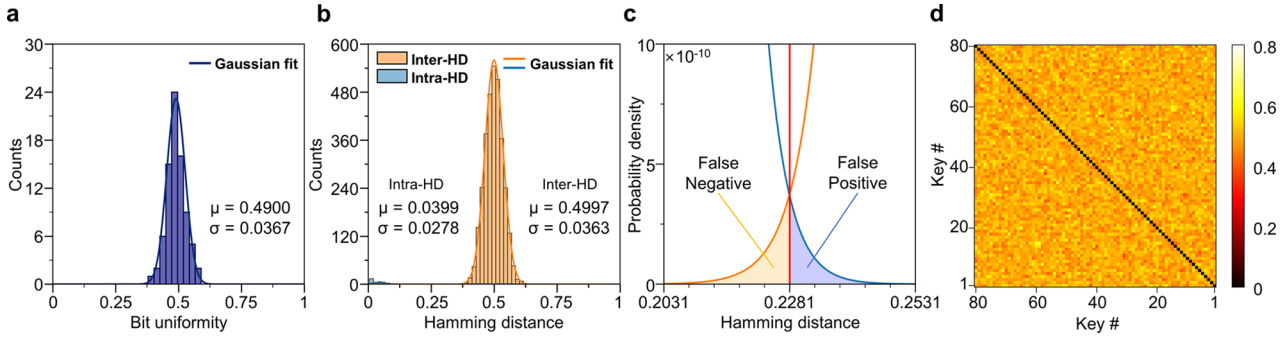

Figure 10. Terms of PUF performances. (a) Distinct value of bit uniformity is driven by summing up all the digit bits and divided into the key length of each sequence. Mean value exhibits a near ideal value, ∼0.5. (b) Intra-HD and inter-HD distributions. To evaluate the intra-HD, the key generation sequence is repeated 36 times. A total of 80 images are compared to determine Inter-HD. Every single full image is assessed for $\sum_{n=0}^{79} n$ = 3160 times. (c) Enlarged intra- and inter-HDs for the authentication threshold. Threshold is 0.2281, which is the crossing point of Gaussian-fitted intra-HD and inter-HD. (d) 2D pair intra-HD. Considering the dense dispersion around the ideal value of 0.5, the maximum value of the matrix plot is set at 0.8. Result of comparing the same key as the black diagonal trace (i.e., value of 0) directed toward the bottom right side in the matrix plot is illustrated.

responses are independent compared to the response at normal incidence (i.e., HD saturates to ∼0.5 at other angles). Consistent with the trend of simulation result, the VSPP-based PUF tag exhibits an excellent angular dependency (Figure S17). Therefore, the PUF system using VSPP tag can implement a strong PUF system by increasing the number of operating wavelengths and/or utilizing oblique light incidence.

2.4. Randomness Evaluation of Extracted Bits. For randomness evaluation of bits, binarized bit sequences are extracted from 20 VSPPs and four different color channels. Each PUF possesses four unique images; hence, the entire response bit size is 15,200 (i.e., 20 × 4 × 190) (Figure 9). The bit uniformity of seed images before the debiasing process, which biased to "0" bits, are shown in Figure S21. The two-channel von Neumann algorithm exploits to equalize the number of 0 and 1 s for each sequence; therefore, the mean value of bit uniformity is 0.4900 (Figure 10a). Intra-HD is calculated for evaluating the repeatability of our system using three images under the wavelengths (i.e., 405, 450, 520, and 638 nm), and estimated for total 36 generation sequences

https://doi.org/10.1021/acsami.2c18737
ACS Appl. Mater. Interfaces XXXX, XXX, XXX−XXX

Table 1. NIST Test Suite Result[a]

statistical NIST test	*p*-value	proportion	result
frequency	0.293235	79/80	true
block frequency	0.199580	79/80	true
cumulative sums	0.414525, 0.013808	79/80, 77/80	true
runs	0.689019	77/80	true
longest run	0.788728	79/80	true
approximate entropy	0.162606	77/80	true
serial	0.834308, 0.964295	76/80, 79/80	true

[a]The collected 15,200 bits are obtained from the statistical NIST test suite. The tests are performed using 80 sequences for 190 bits from the VSPP film. A *p*-value of >0.0001 is determined to true random bitstream for each test. The gathered entire bit sequence is illustrated in Figure S23.

(Figure 10b; blue bins and curve). Figure S22 shows the detailed process for the evaluation of intra-HD. The mean value was 0.0399, which is close to the ideal value of zero. The inter-HD is evaluated for 80 sequences with a mean value of 0.4997 (Figure 10b; orange bins and curves).

Using these estimated intra-/inter-HDs, a threshold of authentication is calculated, which is determined by the overlapping regions of Gaussian fittings of inter-/intra-HDs (Figure 10c). The authentication threshold determines a false positive rate and false negative rate, which are the probability that a wrong PUF successes to be authenticated or a correct PUF fails to be authenticated, respectively.[6,31] Our authentication threshold is 0.2281, and the resulting false positive and negative rates are 1.4850×10^{-12} and 1.7922×10^{-12}, respectively. In addition, the practical encoding capacity of our system is evaluated using "degree of freedom (DoF)". Various PUF systems have investigated their practical encoding capacity by considering independent bit elements in bit sequences.[31] The DoF is given by

$$\mathrm{DoF} = \frac{\mu(1-\mu)}{\sigma^2}$$

where μ is the mean of inter-HD and σ is the standard deviation of inter-HD. Based on this formula, our system shows a DoF of ~190 ($\approx 0.4997 \times (1 - 0.4997)/0.0363^2$)[6] and an encoding capacity of $\sim 2^{190}$ ($\approx 1.57 \times 10^{57}$). Figure 10d shows the pairwise HD for 80 bit sequences. Besides diagonal values, the mean value of pairwise HD is ~0.5; therefore, the individual responses are different bitstreams. Moreover, by valuing the HD, a statistical NIST test suite (NIST SP 800-22)[32] is considered to highlight the randomness of our overall cryptographic system (Table 1). The statistical NIST test suite is used for the collected bitstreams (Figure S23). Therefore, the proposed PUF system can serve as a platform for a strong PUF system if the number of challenges increases by introducing a wavelength-tunable laser and/or a light source with incident angle control. Supporting Note 2 describes the numerical performance estimation method for PUFs.[53]

3. CONCLUSIONS

In summary, we proposed a lens-free, vailed, spectrally unique optical PUF system based on a VSPP tag, which can be fabricated by a simple and affordable process. The hierarchical layers such as saturated and porous layers unable to identify the whole geometries of VSPP using optical and electron microscopy, which increase the security level of the PUF system. Theoretical simulations exhibit that abundant nanopores lead to a multiple Mie scattering and interference causing spectrally different weak light localizations in the porous layer. Moreover, the contrast in the refractive index of PMMA and the air gap are adequate to trigger the scattering. Experimentally, we also optimized the fabrication condition of VSPP by measuring transmittance spectra and testing film formation depending on the composites ratio in the solution. By optical simulations and fabrication optimization, we manufactured an optimum VSPP and demonstrated the wavelength dependency of the VSPP using our lens-less setup. The light−matter interactions were distinct depending on the color channels; hence, the location and intensity of pixel spots in an image sensor varied with the wavelength of the light source (i.e., violet, blue, green, and red). Finally, we confirmed that the VSPP-based PUF system satisfies PUF conditions, e.g., bit uniformity, robustness, uniqueness, and randomness requirements. Although the experimental validations were performed using four wavelengths, the VSPP-based PUF systems possess the potential for a large repertoire of CRP when using a wavelength-tunable light source and/or incident angle-tunable light source. Thus, our system can serve as a strong PUF system. In addition, the modularization of the VSPP-based PUF system can offer the compact and portable truly unclonable security system (Figure S24).

4. METHODS AND EXPERIMENTS

4.1. Bit Extraction Process. The detailed procedure of the two-channel von Neumann extractor is described in Supporting Note 1. The debiasing step was applied to each column bit array of the acquired images. If the length of the debiased column bits was four, the next column was selected as debiased. This process was repeated until the length of the completely extracted bitstream was 190 bits per image. The aforementioned process was performed for every 80 images, and 15,200 response bits were collected to evaluate the NIST test suite ($20 \times 4 \times 190$) (Figure S23).

4.2. Optical Simulation. The computing software used to simulate FDTD in porous media was FullWAVE (RSoft Design Group, Synopsys, United States). The entire data processing was executed using Python 3.9.7 and Jupyter Notebook. The open-source image-processing library OpenCV was used for denoising, resizing, grayscaling, and thresholding raw visual data. The visualized data were treated using the Python plotting libraries, i.e., Matplotlib and Seaborn. The SEM image analysis (i.e., pore diameter and NND (Nearest Neighbor Distance) of each pore) were performed using ImageJ. The surface roughness obtained from the AFM image was measured using Gwyddion.

4.3. Sample Fabrication. The slide glass substrate has 7.6×5.2 cm^2 dimension and the thickness is 1 mm (iNexus, Inc., Republic of Korea). Each glass substrate was cut into 1.5×1.5 cm^2. The diced glass was cleaned with acetone and isopropyl alcohol for 15 min in a sonication bath. After cleaning, nitrogen gas was blown onto the glass surface. Acetone (50 g), PMMA (5 g), and DI water (4 g) were blended and sonicated for 3 h. 1 mL of the fully dissolved solution was spin-coated at 500 rpm for 60 s on a glass substrate and annealed using a hotplate at 120 °C for 5 min.

■ ASSOCIATED CONTENT

Supporting Information

The Supporting Information is available free of charge at https://pubs.acs.org/doi/10.1021/acsami.2c18737.

Methods of the two-channel von Neumann extractor; evaluating the performance of PUFs; recent research trends of optical PUFs; proving the wavelength dependency of Mie scattering; more detailed procedure for the data processing step; micro/nanoscaled quantitative

https://doi.org/10.1021/acsami.2c18737
ACS Appl. Mater. Interfaces XXXX, XXX, XXX−XXX

profiles, theoretical analysis, and experimental results of VSPP; methods of computational calculations; proposal for a compact housing using the VSPP-based PUF system (PDF)

AUTHOR INFORMATION

Corresponding Author

Gil Ju Lee − *Department of Electronics Engineering, Pusan National University, Busan 46241, Republic of Korea;* orcid.org/0000-0003-2225-2738; Email: gjlee0414@pusan.ac.kr

Author

Min Seong Kim − *Department of Electronics Engineering, Pusan National University, Busan 46241, Republic of Korea;* orcid.org/0000-0001-9694-7220

Complete contact information is available at: https://pubs.acs.org/10.1021/acsami.2c18737

Notes

The authors declare no competing financial interest.

ACKNOWLEDGMENTS

This study was supported by the National Research Foundation of Korea (No. NRF-2021R1C1C2013605).

REFERENCES

(1) Arppe-Tabbara, R.; Tabbara, M.; Sørensen, T. J. Versatile and Validated Optical Authentication System Based on Physical Unclonable Functions. *ACS Appl. Mater. Interfaces* **2019**, *11*, 6475−6482.

(2) Chaudhry, P. E. Dupe Influencers Exploiting Social Media to Peddle Luxury Fakes. *Bus. Horiz.* **2022**, *65*, 719−727.

(3) Aini, A. Contributory Infringement and Dupe Influencers. https://cardozoaelj.com/2022/02/21/contributory-infringement-and-dupe-influencers (accessed December 2022).

(4) Song, L.; Meng, Y.; Chang, H.; Li, W.; Tan, K. How Counterfeit Dominance Affects Luxury Fashion Brand Owners' Perceptions: A Cross-Cultural Examination. *J. Bus. Res.* **2021**, *130*, 1−13.

(5) Liang, B. A.; Mackey, T. K. Online Risks to Health—the Problem of Counterfeit Drugs. *Nat. Rev. Urol.* **2012**, *9*, 480−482.

(6) Leem, J. W.; Kim, M. S.; Choi, S. H.; Kim, S.-R.; Kim, S.-W.; Song, Y. M.; Young, R. J.; Kim, Y. L. Edible Unclonable Functions. *Nat. Commun.* **2020**, *11*, 328.

(7) Clark, F. Rise in Online Pharmacies Sees Counterfeit Drugs Go Global. *Lancet* **2015**, *386*, 1327−1328.

(8) Lenstra, A. K.; Verheul, E. R. Selecting Cryptographic Key Sizes. *J. Cryptol.* **2001**, *14*, 255−293.

(9) Ergün, S.; Özoğuz, S. Truly Random Number Generators Based on Non-Autonomous Continuous-Time Chaos. *Int. J. Circ. Theor. Appl.* **2010**, *38*, 1−24.

(10) Dodda, A.; Wali, A.; Wu, Y.; Pannone, A.; Reddy, L. K.; Raha, A.; Ozdemir, S. K.; Ozbolat, I. T.; Das, S. Biological One-Way Functions for Secure Key Generation. *Adv. Theory Simul.* **2019**, *2*, No. 1800154.

(11) Bellare, M.; Rogaway, P. Entity Authentication and Key Distribution. *Adv. Cryptol.—CRYPTO* **1994**, *93*, 232−249.

(12) Yang, J.; Johansson, T. An Overview of Cryptographic Primitives for Possible Use in 5G and Beyond. *Sci. China Inf. Sci.* **2020**, *63*, 220301.

(13) Seo, W.; Pak, W. Real-Time Network Intrusion Prevention System Based on Hybrid Machine Learning. *IEEE Access* **2021**, *9*, 46386−46397.

(14) Razavi, B.; Roghani-Mamaqani, H.; Salami-Kalajahi, M. Development of Highly Sensitive Metal-Ion Chemosensor and Key-Lock Anticounterfeiting Technology Based on Oxazolidine. *Sci. Rep.* **2022**, *12*, 1079.

(15) Taşcıoğlu, D.; Sevim Ünlütürk, S.; Üzçelik, S. An Anti-counterfeiting Technology Combining an InP Nanoparticle Ink and a Versatile Optical Device for Authentication. *Mater. Adv.* **2021**, *2*, 5967−5976.

(16) Kim, M.-S.; Tcho, I.-W.; Park, S.-J.; Choi, Y.-K. Random Number Generator with a Chaotic Wind-Driven Triboelectric Energy Harvester. *Nano Energy* **2020**, *78*, No. 105275.

(17) Garnaev, A.; Trappe, W. A Sophisticated Anti-Eavesdropping Strategy. *IEEE Wirel. Commun. Lett.* **2022**, *11*, 1463−1467.

(18) Lu, X.; Hong, L.; Sengupta, K.15.9 an Integrated Optical Physically Unclonable Function Using Process-Sensitive Sub-Wavelength Photonic Crystals in 65nm CMOS. In *2017 IEEE International Solid-State Circuits Conference (ISSCC)*; 2017.

(19) Pappu, R.; Recht, B.; Taylor, J.; Gershenfeld, N. Physical One-Way Functions. *Science* **2002**, *297*, 2026−2030.

(20) McGrath, T.; Bagci, I. E.; Wang, Z. M.; Roedig, U.; Young, R. J. A PUF Taxonomy. *Appl. Phys. Rev.* **2019**, *6*, No. 011303.

(21) Kim, J.; Yun, J. M.; Jung, J.; Song, H.; Kim, J.-B.; Ihee, H. Anti-Counterfeit Nanoscale Fingerprints Based on Randomly Distributed Nanowires. *Nanotechnology* **2014**, *25*, No. 155303.

(22) Bossuet, L.; Ngo, X. T.; Cherif, Z.; Fischer, V. A PUF Based on a Transient Effect Ring Oscillator and Insensitive to Locking Phenomenon. *IEEE Trans. Emerg. Top. Comput.* **2014**, *2*, 30−36.

(23) Fan, Y.; Zhang, C.; Gao, Z.; Zhou, W.; Hou, Y.; Zhou, Z.; Yao, J.; Zhao, Y. S. Randomly Induced Phase Transformation in Silk Protein-Based Microlaser Arrays for Anticounterfeiting. *Adv. Mater.* **2021**, *33*, No. 2102586.

(24) Dong, H.; Zhang, C.; Zhou, W.; Yao, J.; Zhao, Y. S. Differential Polymer Chain Scission Enables Free-Standing Microcavity Laser Arrays. *Adv. Mater.* **2022**, *34*, No. 2107611.

(25) Kim, J. H.; Jeon, S.; In, J. H.; Nam, S.; Jin, H. M.; Han, K. H.; Yang, G. G.; Choi, H. J.; Kim, K. M.; Shin, J.; Son, S.-W.; Kwon, S. J.; Kim, B. H.; Kim, S. O. Nanoscale Physical Unclonable Function Labels Based on Block Copolymer Self-Assembly. *Nat. Electron.* **2022**, *5*, 433−442.

(26) Mesaritakis, C.; Akriotou, M.; Kapsalis, A.; Grivas, E.; Chaintoutis, C.; Nikas, T.; Syvridis, D. Physical Unclonable Function Based on a Multi-Mode Optical Waveguide. *Sci. Rep.* **2018**, *8*, 9653.

(27) Grubel, B. C.; Bosworth, B. T.; Kossey, M. R.; Sun, H.; Cooper, A. B.; Foster, M. A.; Foster, A. C. Silicon Photonic Physical Unclonable Function. *Opt. Express* **2017**, *25*, 12710.

(28) Wan, Y.; Wang, P.; Huang, F.; Yuan, J.; Li, D.; Chen, K.; Kang, J.; Li, Q.; Zhang, T.; Sun, S.; Qiu, Z.; Yao, Y. Bionic Optical Physical Unclonable Functions for Authentication and Encryption. *J. Mater. Chem. C* **2021**, *9*, 13200−13208.

(29) Hu, Y.; Zhang, T.; Wang, C.; Liu, K.; Sun, Y.; Li, L.; Lv, C.; Liang, Y.; Jiao, F.; Zhao, W.; Dong, L.; Shan, C. Flexible and Biocompatible Physical Unclonable Function Anti-Counterfeiting Label. *Adv. Funct. Mater.* **2021**, *31*, No. 2102108.

(30) Torun, N.; Torun, I.; Sakir, M.; Kalay, M.; Onses, M. S. Physically Unclonable Surfaces via Dewetting of Polymer Thin Films. *ACS Appl. Mater. Interfaces* **2021**, *13*, 11247−11259.

(31) Kim, M. S.; Lee, G. J.; Leem, J. W.; Choi, S.; Kim, Y. L.; Song, Y. M. Revisiting Silk: A Lens-Free Optical Physical Unclonable Function. *Nat. Commun.* **2022**, *13*, 247.

(32) Kang, M. H.; Lee, G. J.; Lee, J. H.; Kim, M. S.; Yan, Z.; Jeong, J.; Jang, K.; Song, Y. M. Outdoor-Useable, Wireless/Battery-Free Patch-Type Tissue Oximeter with Radiative Cooling. *Adv. Sci.* **2021**, *8*, No. 2004885.

(33) Im, H.; Yoon, J.; Choi, J.; Kim, J.; Baek, S.; Park, D. H.; Park, W.; Kim, S. Chaotic Organic Crystal Phosphorescent Patterns for Physical Unclonable Functions. *Adv. Mater.* **2021**, *33*, No. 2102542.

(34) Park, J.; Leem, J. W.; Ku, Z.; Kim, J. O.; Chegal, W. C.; Kang, S.-W.; Kim, Y. L. Disordered Heteronanostructures of MoS_2 and TiO_2 for Unclonable Cryptographic Primitives. *ACS Appl. Nano Mater.* **2021**, *4*, 2076−2085.

(35) John, R. A.; Shah, N.; Vishwanath, S. K.; Ng, S. E.; Febriansyah, B.; Jagadeeswararao, M.; Chang, C.-H.; Basu, A.; Mathews, N. Halide Perovskite Memristors as Flexible and Reconfigurable Physical Unclonable Functions. *Nat. Commun.* **2021**, *12*, 3681.
(36) Park, J.; Kim, T.-H.; Kim, S.; Lee, G. H.; Nili, H.; Kim, H. Conduction Mechanism Effect on Physical Unclonable Function Using Al2O3/TiOX Memristors. *Chaos, Solitons Fractals* **2021**, *152*, No. 111388.
(37) Rahman, A. Nano-and Micro-Features on Semiconductor Chips Measured via Terahertz Reconstructive Imaging Route. *Novel Res. Sci.* **2019**, *1*, 1−4.
(38) Sauermann, K.; Clemann, S.; Jaspers, S.; Gambichler, T.; Altmeyer, P.; Hoffmann, K.; Ennen, J. Age Related Changes of Human Skin Investigated with Histometric Measurements by Confocal Laser Scanning Microscopy in Vivo. *Skin Res. Technol.* **2002**, *8*, 52−56.
(39) Yakimov, B. P.; Gurfinkel, Y. I.; Davydov, D. A.; Allenova, A. S.; Budylin, G. S.; Vasiliev, V. Y.; Soldatova, V. Y.; Kamalov, A. A.; Matskeplishvili, S. T.; Priezzhev, A. V.; Shirshin, E. A. Pericapillary Edema Assessment by Means of the Nailfold Capillaroscopy and Laser Scanning Microscopy. *Diagnostics* **2020**, *10*, 1107.
(40) Sinem Bağcı, I.; Aoki, R.; Vladimirova, G.; Ergün, E.; Ruzicka, T.; Sárdy, M.; French, L. E.; Hartmann, D. New-Generation Diagnostics in Inflammatory Skin Diseases: Immunofluorescence and Histopathological Assessment Using Ex Vivo Confocal Laser Scanning Microscopy in Cutaneous Lupus Erythematosus. *Exp. Dermatol.* **2021**, *30*, 684−690.
(41) Du, H. Mie-Scattering Calculation. *Appl. Opt.* **2004**, *43*, 1951.
(42) Nussenzveig, H. M.; Wiscombe, W. J. Efficiency Factors in Mie Scattering. *Phys. Rev. Lett.* **1980**, *45*, 1490−1494.
(43) Buades, A.; Coll, B.; Morel, J.Image Denoising by Non-Local Averaging. In *Proceedings (ICASSP '05). IEEE International Conference on Acoustics, Speech, and Signal Processing, 2005*; 2005, vol *2*.
(44) Mandal, J.; Fu, Y.; Overvig, A. C.; Jia, M.; Sun, K.; Shi, N. N.; Zhou, H.; Xiao, X.; Yu, N.; Yang, Y. Hierarchically Porous Polymer Coatings for Highly Efficient Passive Daytime Radiative Cooling. *Science* **2018**, *362*, 315−319.
(45) Cheng, W.; Richter, M. H.; Müller, R.; Kelzenberg, M.; Yalamanchili, S.; Jahelka, P. R.; Perry, A. N.; Wu, P. C.; Saive, R.; Dimroth, F.; Brunschwig, B. S.; Hannappel, T.; Atwater, H. A. Integrated Solar-Driven Device with a Front Surface Semitransparent Catalysts for Unassisted CO_2 Reduction (Adv. Energy Mater. 36/2022). *Adv. Energy Mater.* **2022**, *12*, No. 2270153.
(46) Prashant, D. V.; Samajdar, D. P.; Arefinia, Z. FDTD-Based Optimization of Geometrical Parameters and Material Properties for GaAs-Truncated Nanopyramid Solar Cells. *IEEE Trans. Electron Devices* **2021**, *68*, 1135−1141.
(47) Tran, T. B.; AlQatari, F.; Luc, Q.-H. Nanophotonic Crystals on Unpolished Sapphire Substrates for Deep-UV Light-Emitting Diodes. *Sci. Rep.* **2021**, *11*, 4981.
(48) Gao, Y.; Cansizoglu, H.; Polat, K. G.; Ghandiparsi, S.; Kaya, A.; Mamtaz, H. H.; Mayet, A. S.; Wang, Y.; Zhang, X.; Yamada, T.; Devine, E. P.; Elrefaie, A. F.; Wang, S.-Y.; Islam, M. S. Photon-Trapping Microstructures Enable High-Speed High-Efficiency Silicon Photodiodes. *Nat. Photonics* **2017**, *11*, 301−308.
(49) Wiersma, D. S.; Bartolini, P.; Lagendijk, A.; Righini, R. Localization of Light in a Disordered Medium. *Nature* **1997**, *390*, 671−673.
(50) Xu, H.; Deng, Y. Dependent Evidence Combination Based on Shearman Coefficient and Pearson Coefficient. *IEEE Access* **2018**, *6*, 11634−11640.
(51) Littrow≫ Tunable Diode Lasers≫ Scientific Lasers≫ Home | Sacher Lasertechnik Group. https://www.sacher-laser.com/home/scientific-lasers/tunable_lasers/littrow/tec-100-tec_120_littrow_laser_system_lynx.html.
(52) Q-TUNE: Tunable DPSS laser. https://www.rpmclasers.com/product/q-tune-tunable-dpss-laser/.
(53) Helinski, R.*Evaluating Physical Unclonable Functions*; 2020.

https://doi.org/10.1021/acsami.2c18737
ACS Appl. Mater. Interfaces XXXX, XXX, XXX−XXX